JACS
JOURNAL OF THE AMERICAN CHEMICAL SOCIETY

ARTICLE

pubs.acs.org/JACS

Autocatalytic O_2 Cleavage by an OCO^{3-} Trianionic Pincer Cr^{III} Complex: Isolation and Characterization of the Autocatalytic Intermediate $[Cr^{IV}]_2(\mu\text{-}O)$ Dimer

Matthew E. O'Reilly,[†] Trevor J. Del Castillo,[†] Joseph M. Falkowski,[†] Vasanth Ramachandran,[‡] Mekhala Pati,[‡] Marie C. Correia,[†] Khalil A. Abboud,[†] Naresh S. Dalal,[‡] David E. Richardson,[†] and Adam S. Veige[*,†]

[†]Department of Chemistry, Center for Catalysis, University of Florida, P.O. Box 117200, Gainesville, Florida 32611, United States

[‡]Department of Chemistry and Biochemistry, Florida State University, Tallahassee, Florida 32306, United States

S *Supporting Information*

ABSTRACT: Synthetic and kinetic experiments designed to probe the mechanism of O_2 activation by the trianionic pincer chromium(III) complex $[{}^tBuOCO]Cr^{III}(THF)_3$ (**1**) (where ${}^tBuOCO = [2,6\text{-}({}^tBuC_6H_3O)_2C_6H_3]^{3-}$, THF = tetrahydrofuran) are described. Whereas analogous porphyrin and corrole oxidation catalysts can become inactive toward O_2 activation upon dimerization (forming a μ-oxo species) or product inhibition, complex **1** becomes more active toward O_2 activation when dimerized. The product from O_2 activation, $[{}^tBuOCO]Cr^V(O)(THF)$ (**2**), catalyzes the oxidation of **1** via formation of the μ-O dimer $\{[{}^tBuOCO]Cr^{IV}(THF)\}_2(\mu\text{-}O)$ (**3**). Complex **3** exists in equilibrium with **1** and **2** and thus could not be isolated in pure form. However, single crystals of **3** and **1** co-deposit, and the molecular stucture of **3** was determined using single-crystal X-ray crystallography methods. Variable (9.5, 35, and 240 GHz) frequency electron paramagnetic resonance spectroscopy supports the assignment of complex **3** as a $Cr^{IV}-O-Cr^{IV}$ dimer, with a high ($S = 2$) spin ground state, based on detailed computer simulations. Complex **3** is the first conclusively assigned example of a complex containing a Cr(IV) dimer; its spin Hamiltonian parameters are $g_{iso} = 1.976$, $D = 2400$ G, and $E = 750$ G. The reaction of **1** with O_2 was monitored by UV−visible spectrophotometry, and the kinetic orders of the reagents were determined. The reaction does not exhibit first-order behavior with respect to the concentrations of complex **1** and O_2. Altering the THF concentration reveals an inverse order behavior in THF. A proposed autocatalytic mechanism, with **3** as the key intermediate, was employed in numerical simulations of concentration versus time decay plots, and the individual rate constants were calculated. The simulations agree well with the experimental observations. The acceleration is not unique to **2**; for example, the presence of $OPPh_3$ accelerates O_2 activation by forming the five-coordinate complex *trans*-$[{}^tBuOCO]Cr^{III}(OPPh_3)_2$ (**4**).

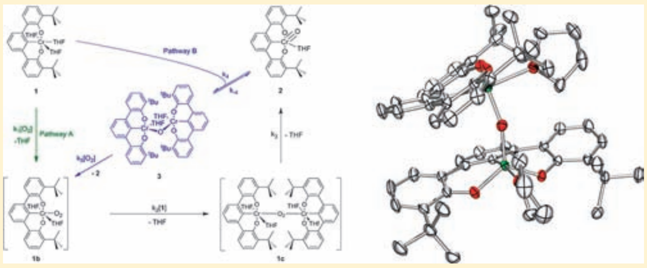

INTRODUCTION

The vast majority of commercial chemicals originate from crude oil.[1−3] An important step in chemical refinement involves selective oxidation to transform the raw materials into useful reagents for further upstream derivation and application.[3−5] Oxygen (O_2) is the most benign and economical oxidant, especially if water is the solvent medium,[6] but autoxidation is inherently unselective. One method of selective oxidation involves the use of transition metal complexes[7−9] to mediate redox equivalents (oxidase)[10−21] or to cleave dioxygen and deliver one (monooxygenase)[9,22−27] or both oxygen atoms (dioxygenase)[9,23,28] to the substrate. Oxygen atom transfer (OAT)[29−33] catalysis presents some unique challenges.[34] A metal catalyst must be reducing enough to bind and cleave O_2 without overoxidation yet the resulting M−oxo complex sufficiently oxidizing enough to transfer the O-atom to substrate.[35,36] For practical applications, maximizing the rate of O_2 cleavage is important but not at the cost of creating inert M−oxo intermediates.[37]

During oxidation catalysis, comproportionation of M^{n+} and $M^{(n+2)+}{=}O$ species can result in thermodynamically stable μ-oxo complexes that do not partipate in catalytic turnover.[33,35,38−40] M−O−M species are known for iron,[41−52] chromium,[39,53−59] and manganese[40,60−74] oxidation catalysts. Of that group, formation of $(P)Fe^{III}-O-Fe^{III}(P)$ (P = porphyrin)[75] can be fatal,[41−44] whereas Cr−O−Cr and Mn−O−Mn complexes form reversibly during catalytic turnover. Although experimental data characterizing such postulated Cr and Mn intermediates exist, structural data are decidedly absent. For $[(salen)Mn^{IV}]_2(\mu\text{-}O)$ intermediates that form during epoxidation of alkenes, characterization relies mainly on mass spectrometry data,[62,65−67] although ^1H NMR[63,64] and UV−vis[74] data have been obtained. Few structural details of relevant species are available; $[(N_3)(P)Mn^{IV}]_2(\mu\text{-}O)$[72,73] is the lone example derived from a known oxidation catalyst. Noncatalytic linear Mn−O−Mn complexes have been structurally characterized

Received: June 8, 2011
Published: July 22, 2011

Scheme 1. General Mechanism for Substrate Oxidation that Includes Reversible Formation of a M−O−M Intermediate

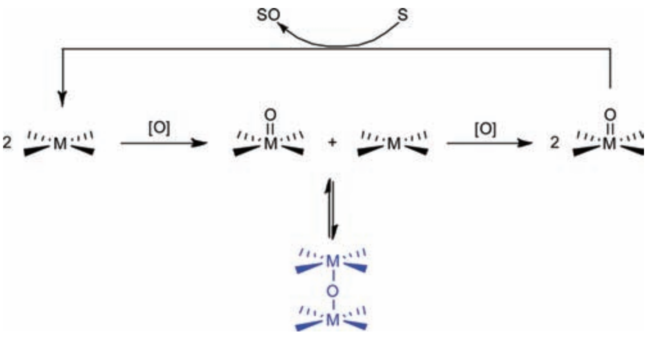

with Mn in the +2/+2,[76] +3/+3,[77−82] +3/+4,[77] and +4/+4[72,73,80,83,84] oxidation states. Similarly for (L)Cr−O−Cr(L) (L = salen or por) intermediates that form during catalysis, the primary characterization data are mass spectrometric.[56,58] A defining characteristic of most linear Cr−O−Cr and Mn−O−Mn units is a strong Soret band (ε = 1000−4000 M^{-1} cm^{-1}).[72,74,77,80,82,83,85−87] X-ray characterization of linear Cr−O−Cr complexes is known for Cr in the +2/+3,[88] +3/+3,[85,86] +3/+4,[89] and +5/+5[90,91] oxidation states, but none of these compounds are oxidation catalysts. Characterization data for a catalytically competent Cr−O−Cr species come from Talsi and co-workers for the dinuclear complex (salen)Cr^{III}OCr^{V}(salen),[57] which forms upon oxidation of (salen)Cr^{III} with 0.5 equiv of iodosobenzene (PhIO). The electron paramagnetic resonance (EPR) spectrum of (salen)Cr^{III}OCr^{V}(salen) exhibits a typical d^1 absorption at $g = 1.976$.

Scheme 1 depicts a typical catalytic cycle for substrate oxidation that includes a M−O−M intermediate. Comproportionation of (L)M and (L)M═O during the initial oxidation stage provides the M−O−M intermediate that inhibits but does not prevent OAT and further oxidation. Excess oxidant[54] converts M−O−M to the mononuclear M═O complex, which oxidizes substrate. Strong σ-donor ligands tend to promote dissociation of such μ-O dimers—notable examples include [(L)Mn^{IV}]$_2$(μ-O) and [(L)Cr^{IV}]$_2$(μ-O)[38,57,68,87]—but in certain cases donor ligands can actually favor formation of the dimer, as in the case of [(P)Fe^{III}]$_2$(μ-O).[58,62,65] Although addition of donor ligands may seem to be a viable option to prevent μ-O formation, excess donor ligand will ultimately impede reoxidation by blocking access of the terminal oxidant to the metal center.[53,87]

Catalyst deactivation of tetradentate catalysts (e.g., porphyrin, corrole, and salen) by product inhibition is common. The inhibition may appear in the form of oxidized substrate binding to the catalyst, or as in the case of M−O−M formation, the oxidized catalyst itself can inhibit. In either case, a product from oxidation inhibits catalysis. Trianionic pincer ligands[92−103] have applications in metal-catalyzed aerobic oxidation,[95] polyolefin synthesis,[97] and N-atom transfer.[100] One potential advatage of trianionic pincer ligands is the presence of a strong metal carbon bond, which is fixed relative to the other anionic pendant donors. As a consequence, substrate or other ligands opposite the M−C bond will experience a strong *trans* influence, which can be exploited to enhance reactivity. In this study, we present evidence for an unprecedented metal-mediated *autocatalytic* O_2 cleavage. In other words, the oxidized product accelerates O_2 cleavage, in contrast to M−O−M species that traditionally inhibit.

For decades, researchers proposed that Cr−O−Cr dimer species form during the epoxidation of olefins; however, no complexes were isolable, and solution characterization is weak. We present the first crystallographically characterized Cr^{IV}−O−Cr^{IV} intermediate from a catalytically relevant system. Specifically, [^{t}BuOCO]Cr^{V}(O)(THF) (**2**) autocatalyzes the oxidation of [^{t}BuOCO]Cr^{III}(THF)$_3$ (**1**) via formation of the highly reactive hitherto unknown Cr^{IV}Cr^{IV} dimer {[^{t}BuOCO]Cr^{IV}(THF)}$_2$(μ-O) (**3**). In addition, we present the first EPR spectrum of a d^2−d^2, Cr^{IV}−O−Cr^{IV} complex, thus providing a definitive spectral signature for these illusive catalytic intermediates.

RESULTS AND DISCUSSION

O_2 Activation by [^{t}BuOCO]Cr^{III}(THF)$_3$ (1). UV−visible spectrophotometry is a suitable method for studying the reaction of [^{t}BuOCO]Cr^{III}(THF)$_3$ (**1**) with O_2. Figure 1 depicts the time-dependent changes in absorption upon exposure of a 1×10^{-4} M solution of **1** to 1.66×10^{-3} M O_2. Control of the O_2 concentration requires injection of a known quantity of an O_2-saturated THF solution (9.90×10^{-3} M at 25 °C).[104] A color change from green to reddish brown occurs when **1** reacts with O_2 to form the Cr^{V}(O) complex [^{t}BuOCO]Cr^{V}(O)(THF) (**2**; Scheme 2).[95,105−114] Changes in the UV−vis spectrum display isosbestic points at 318 and 385 nm, and measuring the changes in the absorption at 341 nm generates a plot of the concentration of **1** vs time (Figure 2).

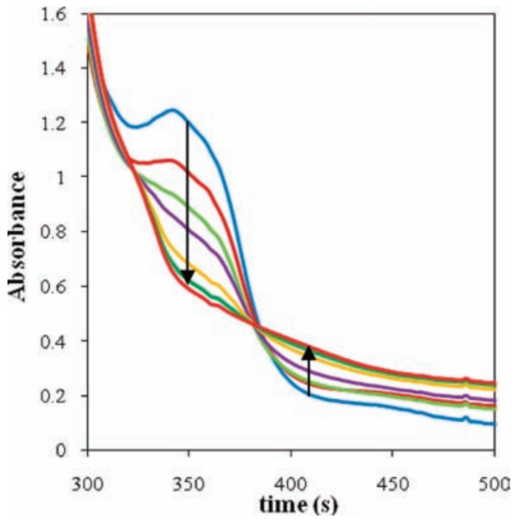

Figure 1. UV−vis spectral change of **1** in THF upon addition of O_2 (25 °C).

Scheme 2. Oxidation of 1 by O_2 to Form 2

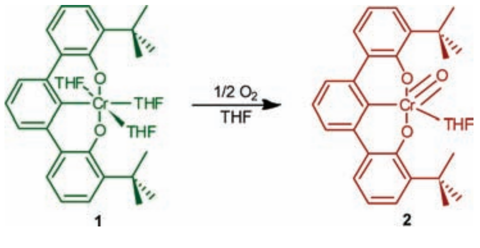

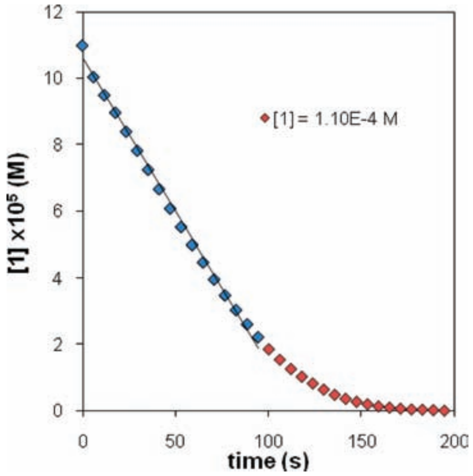

Figure 2. Concentration vs time (s) for the oxidation of **1** by O_2 in THF; within 1st 80% (blue), after 80% (red) (25 °C).

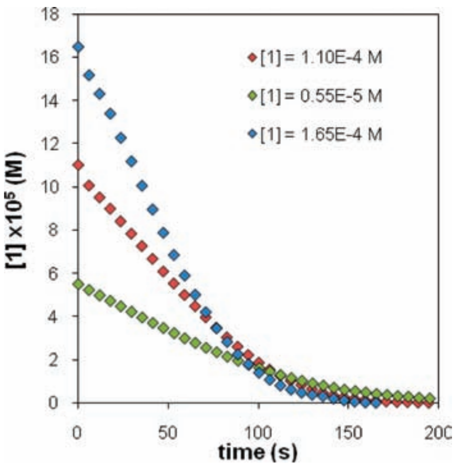

Figure 3. Concentration (**1**) vs time (s) for the oxidation of **1** (0.55−1.65 ($\times 10^{-4}$) M) with O_2 (1.66×10^{-3} M) in THF (25 °C).

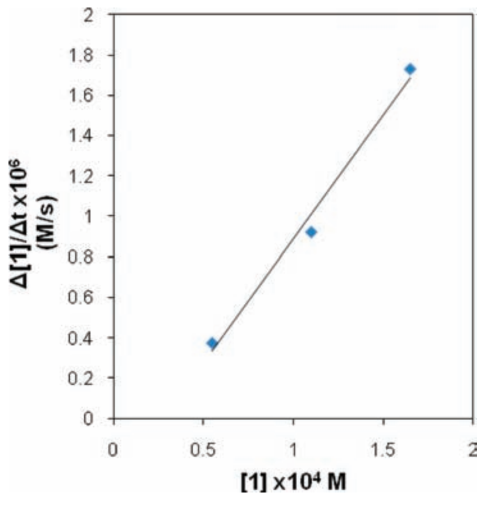

Figure 4. Plot of $-\Delta[\mathbf{1}]/\Delta t$ vs $[\mathbf{1}]$ ($[\mathbf{1}] = 0.55-1.65$ ($\times 10^{-4}$) M; $[O_2] = 1.66 \times 10^{-3}$ M (THF, 25 °C)).

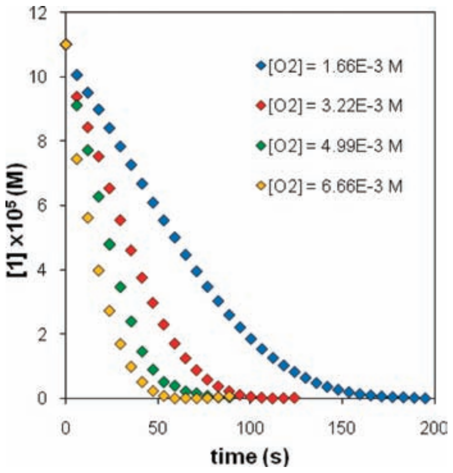

Figure 5. Concentration (**1**) vs time (s) for the oxidation of **1** (1.10×10^{-4} M) with O_2 (1.66−6.66 ($\times 10^{-3}$) M) in THF (25 °C).

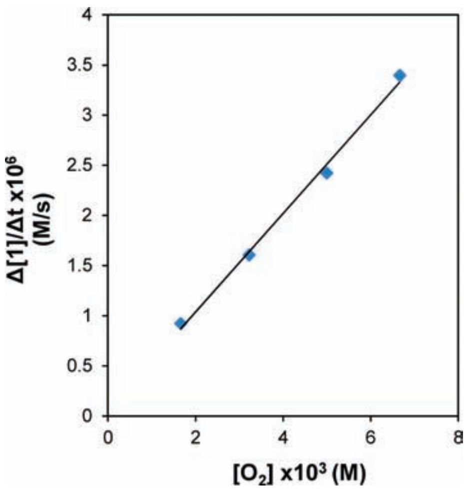

Figure 6. Plot of rate $-\Delta[\mathbf{1}]/\Delta t$ vs $[O_2]$ ($[\mathbf{1}] = 1.10 \times 10^{-4}$ M; $[O_2] = 1.66-6.66$ ($\times 10^{-4}$) M) in THF (25 °C).

The complete oxidation of **1** occurs within approximately three minutes. Plots of concentration vs time reveal a linear segment within the first ~80% of the reaction, followed by a gradual curvature in the remainder of the reaction until completion (Figure 2). The plot of [**1**] vs time does not fit first-order or second-order kinetics.

O_2 Cleavage Rate Dependence on [1], [O_2], [THF], and Temperature. Solutions of **1**, between 0.55 and 1.65 ($\times 10^{-4}$) M, were allowed to react with O_2 and result in the concentration versus time plots in Figure 3.

The initial rates can be determined from the initial values of $\Delta[\mathbf{1}]/\Delta t$. Figure 4 shows the linear dependence of the average rate, $\Delta[\mathbf{1}]/\Delta t$, on the [**1**]. The linear plot indicates a first-order dependence on [**1**].

Determination of the order in O_2 requires addition of known quantities of O_2-saturated THF solutions to **1**. The concentration of O_2 in a saturated THF solution is 9.90×10^{-3} M.[104] Four independent reactions that vary in O_2 concentration from 1.66 to 6.66 mM (Figure 5) result in a linear plot of initial rate $\Delta[\mathbf{1}]/\Delta t$ versus [O_2] (Figure 6). The linear dependence indicates a first-order O_2 relationship.

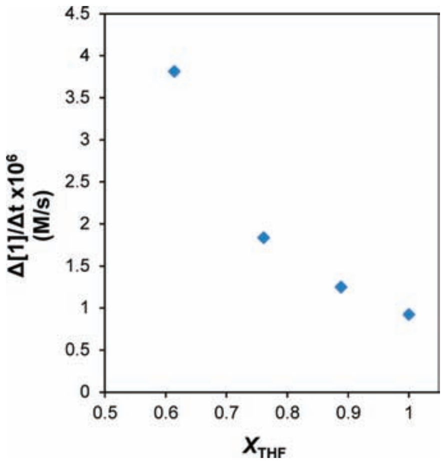

Figure 7. Plot of rate $-\Delta[\mathbf{1}]/\Delta t$ vs X_{THF} ($[\mathbf{1}] = 1.10 \times 10^{-4}$ M; $[O_2] = 1.66 \times 10^{-3}$ M; THF/hexane (mL:mL) = 2.5:0.5, 2.0:1.0, 1.5:1.5) at 25 °C.

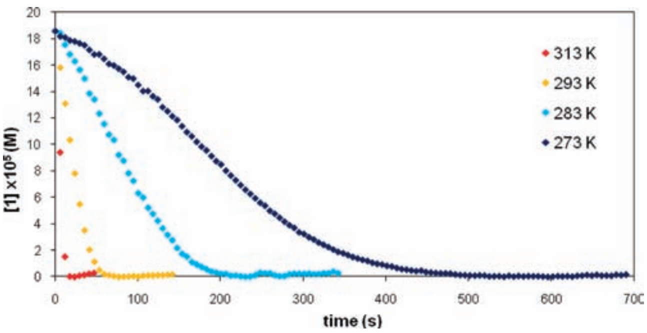

Figure 8. Concentration of **1** (1.84×10^{-4} M) vs time in THF upon addition of O_2 (1.66×10^{-3} M) at 40 °C (red), 20 °C (yellow), 10 °C (light blue), and 0 °C (dark blue).

The oxidation of **1** with O_2 in noncoordinating solvents proceeds rapidly. The complete oxidation of **1** in hexanes occurs within ~3 s, thus preventing the measurement of a reliable reaction rate. Introduction of THF between 50% and 100% (v/v) into a hexanes solution of **1** slows the reaction enough to permit the determination of $\Delta[\mathbf{1}]/\Delta t$ and thus the solvent's role. Plotting $-\Delta[\mathbf{1}]/\Delta t$ vs X_{THF} yields a parabolic curve (Figure 7) consistent with an inverse order in [THF]. However, changes in the dielectric constant of the different solvent mixture can also produce a similar effect, thus assigning a *specific* order to the inverse relation in THF is not possible.

Lowering the temperature of the reaction provides more insight into the unusual nonfirst-order kinetic profile by resolving the shape of the decay plot of [**1**] vs time. Figure 8 depicts the [**1**] vs time plot at 40, 20, 10, and 0 °C. The kinetic trial at 0 °C yields a sigmoidal plot of [**1**] vs time, which is consistent with an autocatalytic mechanism.

If the oxidation of **1** is catalyzed by **2**, then increasing the initial [**2**] should accelerate O_2 activation. Figures 9 and 10 depict an increasing rate of oxidation of **1** with an increasing initial [**2**] and confirm the product-catalyzed oxidation of **1**.

We propose that the oxidation of **1** by O_2 occurs via an autocatalytic mechanism. Initially, the oxidation of **1** to **2** is slow. However, upon accumulation of **2** in solution, a faster autocatalytic

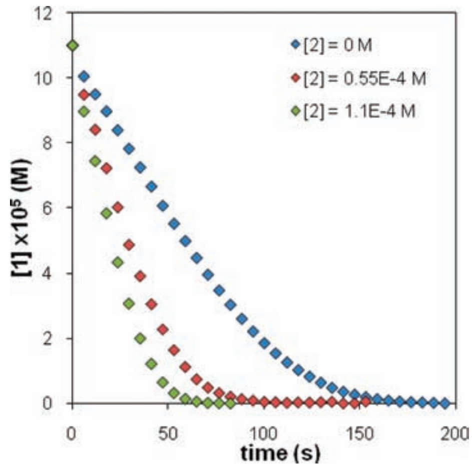

Figure 9. Concentration of **1** vs time (s) for the oxidation of **1** (1.10×10^{-4} M) by O_2 (1.66×10^{-3} M) with increasing [**2**] (0, 5.5×10^{-5}, and 1.10×10^{-5} M) in THF (25 °C).

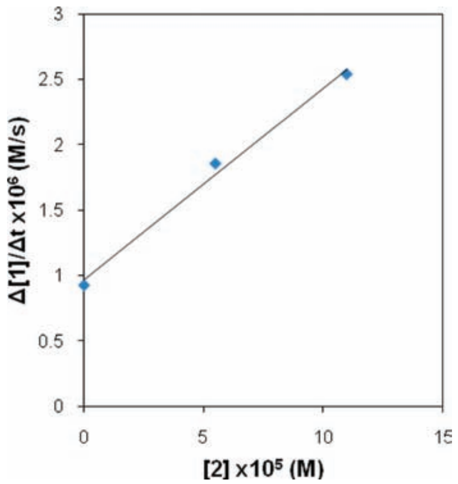

Figure 10. Plot of $\Delta[\mathbf{1}]/\Delta t$ for the oxidation of **1** (1.10×10^{-4} M) by O_2 (1.66×10^{-3} M) with increasing [**2**] (0, 0.55×10^{-4}, and 1.10×10^{-4} M) in THF (25 °C).

pathway, in which the product **2** catalyzes the oxidation of **1** to **2**, becomes predominant (vide infra).

Characterization of the Autocatalytic Intermediate: The Chromium(IV) μ-oxo Dimer $\{[{}^t\mathrm{BuOCO}]\mathrm{Cr}^{\mathrm{IV}}(\mathrm{THF})\}_2(\mu\text{-O})$ (3). How does $[{}^t\mathrm{BuOCO}]\mathrm{Cr(O)(THF)}$ (**2**) catalyze O_2 activation by **1**? One possibility is the formation of a $\mathrm{Cr^{IV}{-}O{-}Cr^{IV}}$ adduct that reacts more rapidly than **1** with O_2. An attempt to form the adduct by stoichiometric addition of **2** to **1** in THF failed. Adding a green solution of **1** and a red solution of **2** in THF yields a brown solution. The ^{1}H NMR spectrum of the reaction mixture reveals only signals attributable to **1** and **2**, and at −35 °C, only green crystals of **1** precipitate. When **1** is oxidized to **2** in toluene, however, a bright purple intermediate species forms and then converts to the deep red color of **2**. Considering this observation, stoichiometric addition of **1** to **2** in toluene indeed yields a bright purple solution consisting of a small concentration of starting reagents and the major product, postulated to be the dimer $\{[{}^t\mathrm{BuOCO}]\mathrm{Cr}^{\mathrm{IV}}(\mathrm{THF})\}_2(\mu\text{-O})$ (**3**) (Scheme 3). The ^{1}H NMR spectrum of the reaction mixture (C_6D_6) contains new paramagnetic

Scheme 3. Equilibrium between Starting Materials 1 and 2 and the Dimer Adduct 3

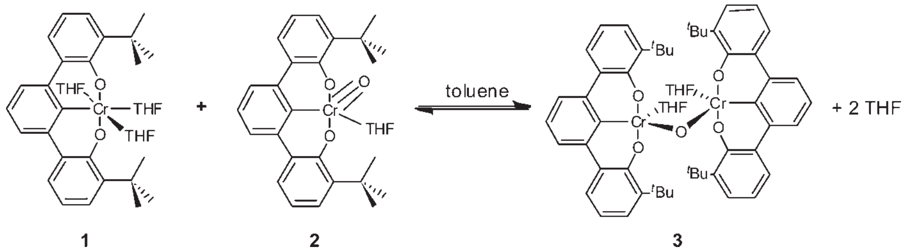

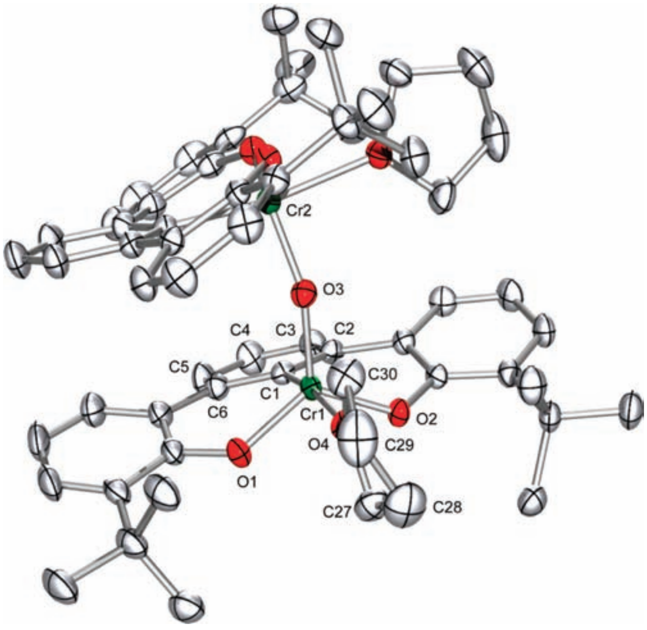

Figure 11. Molecular structure of $\{[^t\mathrm{BuOCO}]\mathrm{Cr}^{\mathrm{IV}}(\mathrm{THF})\}_2\mathrm{O}$ (**3**) with ellipsoids drawn at the 50% probability level and hydrogen atoms and an ether lattice molecule removed for clarity.

resonances distinct from **1** and **2** at 28.70 ($\nu_{1/2}$ = 570 Hz), 16.89 ($\nu_{1/2}$ = 675 Hz), and −30.57 ($\nu_{1/2}$ = 540 Hz) ppm. The characteristic ^{1}H NMR signals for **3** disappear upon addition of THF, indicating that an equilibrium exists between Cr$^{\mathrm{III}}$ (**1**) and Cr$^{\mathrm{V}}$(O) (**2**) and **3**. The formation of **3** evidently requires a noncoordinating solvent.

Purple hexagonal-plate single crystals of **3** form at −35 °C from concentrated diethyl ether solutions of the mixture. Since **1** is present in the equilibrium mixture, several crystals of **1** also deposit, and as a result, isolation of pure **3**, except as a single crystal, is not possible. Subjecting the purple crystals to a single-crystal X-ray analysis experiment provides the molecular structure of **3**. In the solid state, complex **3** is C_2 symmetric and contains two [^{t}BuOCO]Cr fragments bridged by oxygen (Figure 11). The asymmetric unit consists of one-half of the molecule, and the O atom resides on a C_2 axis that generates the second half of the molecule, thus rendering the Cr ions equidistant from the μ-oxo by 1.7497(6) Å and creating a 158.69(14)° Cr−O−Cr angle across the bridge. As a consequence, the Cr−O bond lengths do not provide insight to ascertain the Cr oxidation state. The geometry of the Cr$^{\mathrm{IV}}$ ion is distorted trigonal bipyramidal (tbp) with an Addison parameter of τ = 0.77.[115]

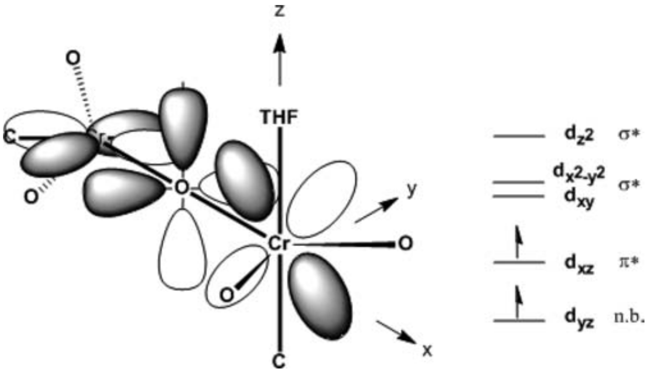

Figure 12. π-Bonding MO and ligand field splitting diagram of the Cr$^{\mathrm{IV}}$ ion in **3**.

Bound to each Cr ion is a trianionic OCO^{3-} pincer, the μ-oxo bridge, and a THF molecule. The equatorial sites consist of the alkoxide attachments and the μ-oxo bridge, whereas the Cr−C$_{ipso}$ bond and THF occupy axial positions. Consistent with a higher oxidation state Cr$^{\mathrm{IV}}$ ion, the Cr−O$_{\mathrm{alkoxide}}$ (d(Cr1−O$_{\mathrm{alkoxide}}$)$_{\mathrm{avg}}$ = 1.8046(2) Å) bonds are shorter than in **1** by 0.113(3) Å, and the Cr−C$_{ipso}$ (d(Cr1−C1) = 1.983(2) Å) is shorter by 0.028(4) Å.

An interesting feature of the structure is the ~82° twist between the two Cr ion coordination environments. Figure 12 provides an electronic argument for the approximate 90° twist and the near linearity of the Cr−O−Cr bonds. The sp-hybridized oxygen forms two σ bonds between the Cr ions. The additional four electrons on oxygen π-donate into Cr d-orbitals. From Figure 12, assigning the C$_{ipso}$−Cr−THF as the z-axis and Cr−O−Cr as the x-axis, the d_{xz} and d_{xy} are two available d-orbitals with appropriate symmetry for accepting π-electrons from oxygen. Since the d_{xy} orbital participates in bonding with the two alkoxide ligands, it is high in energy and relatively inaccessible. In contrast, the d_{xz} orbital is a low-lying energy orbital available for π-bonding with oxygen. The most favorable π-donating interaction is into the d_{xz} of each respective Cr ion, thus adopting a ~90° twist to accommodate the two orthogonal lone pairs on the oxygen. Figure 12 also depicts a ligand field splitting diagram that corresponds to this bonding and electronic interaction. Assigning two d-electrons to the d_{xz} and d_{yz} orbitals of each Cr center allows for the maximum number of unpaired electrons. A similar assignment was made for an isoelectronic V$^{\mathrm{III}}$−O−V$^{\mathrm{III}}$ dimer.[116] The resulting d^2 configuration for each Cr ion supports an oxidation state of +4 for each ion. Despite the smaller Cr$^{\mathrm{IV}}$ ion, the Cr−THF distance is 0.043(2) Å longer than that in **1**, due to the stronger *trans* influence of the Cr−C$_{ipso}$ bond in **3** and a more congested coordination sphere due to the mutually adjacent [^{t}BuOCO]Cr$^{\mathrm{IV}}$ fragment.

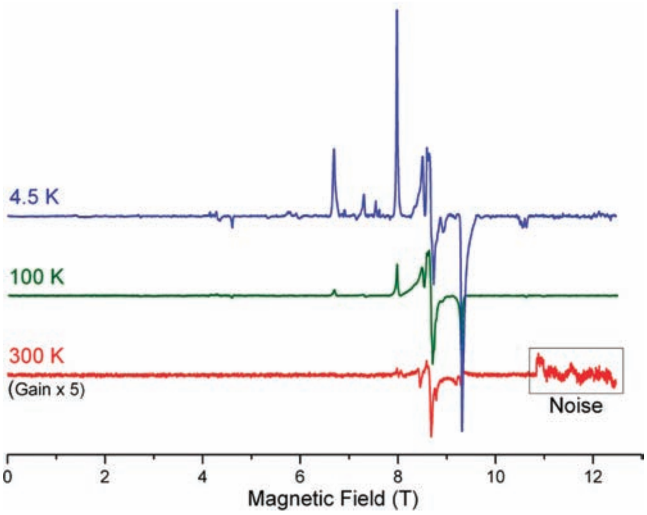

Figure 13. Variable-temperature high-frequency (240 GHz) powder EPR spectra of major **3** and minor **1**. The boxed part of the spectrum at 300 K is due to the noise from the spectrometer electronics.

Electron Paramagnetic Resonance Measurements. Though the above X-ray and NMR results indicated that **3** is a new paramagnetic Cr−O−Cr dimer, additional data were needed to characterize its electronic structure. Figure 13 depicts the 240 GHz EPR spectra of a powder sample of **3**. The resonances indicate the presence of Cr(III) (weak signals) and a $S = 2$ dimer (**3**). Reducing the temperature lowers the thermal Boltzmann population of electronic states, and the resonances intensify (Figure 13). The program SPIN[117] simulates the EPR spectrum at 4.5 K, and for comparison, Figure 14 depicts both the simulated spectrum and experimental data. Simulating the $Cr^{IV}-O-Cr^{IV}$ species alone did not reproduce all the resonances. Considering that **3** is in equilibrium with the mononuclear complexes **1** and **2** (Scheme 3), complex **1** was included in the simulation. However, complex **2** is difficult to distinguish among resonances 5, 6, and 7 of Figure 14 and is present in less than 10%. Thus, it was not included in the simulation. The resonances arise from the predominant (∼70%) $S = 2$ ($Cr^{IV}-O-Cr^{IV}$, **3**) and the minor component $S = 1.5$ (Cr^{III}, **2**). For the dinuclear complex **3**, the two paramagnetic fragments, with spins S_1 and S_2, can be described by the following standard spin Hamiltonian,[118−120] where

$$H = JS_1 \cdot S_2 + \beta H \cdot \bar{g} \cdot S + D\left(S_z^2 - \frac{S(S+1)}{3}\right) + E(S_x^2 - S_y^2) + H_{hyp} \quad (1)$$

J is the spin-exchange coupling constant; β is the Bohr magneton; $\bar{g}$ is the Lande g-tensor; S is the total spin = $S_1 + S_2$, with components S_x, S_y, and S_z, with z being taken to be the direction along which the Zeeman field H is applied. H_{hyp} is the electron−nuclear hyperfine interaction. The EPR spectrum reveals no hyperfine splitting from the ^{53}Cr isotope (9.5% abundant) with $I = 3/2$, so H_{hyp} can be omitted. The spin Hamiltonian parameters for $S = 2$ ($Cr^{IV}-O-Cr^{IV}$) $g_{iso} = 1.976$, $D = 2400$ G (Gauss), and $E = 750$ G and for $S = 1.5$ (Cr^{III}) are $g_{iso} = 1.976$, $D = 10\,500$ G (Gauss), and $E = 3000$ G (Figure 14). The good fit of the simulation to the experimental spectrum permits conclusive assignment of a +4 (d^2) oxidation state for each Cr ion in **3**. The individual simulations for the $Cr^{IV}-O-Cr^{IV}$ dimer and Cr^{III} species are in the Supporting Information.

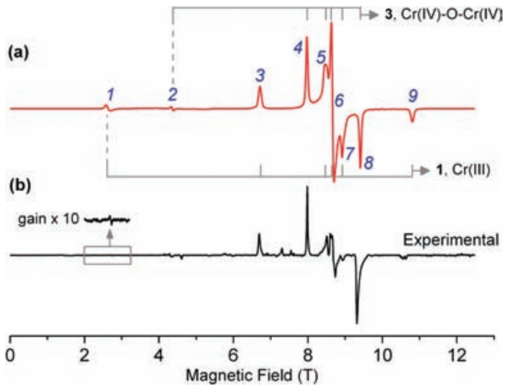

Figure 14. Simulated (a) and experimental (b) powder EPR spectra of **3** and **1** at 240 GHz and 4.5 K. The simulated spectrum (b) is the sum of the individually simulated spectra of **3** and **1**. Peak assignments. Complex **1** ($S = 1.5$): allowed transitions = 3, 5, 6, 7 and 9; forbidden transition =1. Complex **3** ($S = 2$): allowed transitions = 4, 5, 6, 7, and 8; forbidden transition = 2. The resonances 5, 6, and 7 are overlapping signals from both **1** and **3** (present in a ratio 1:2.5).

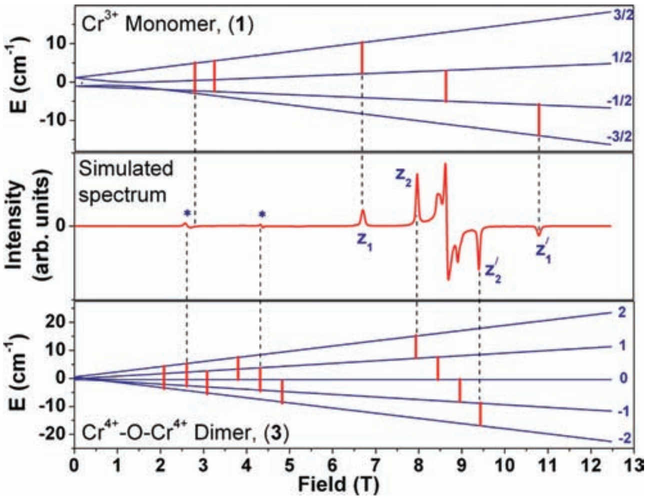

Figure 15. Simulated 240 GHz energy level diagram and EPR spectrum of **3** + **1** (2.5:1 ratio), at 4.5 K. Middle panel: simulated spectrum corresponding to the sum of individual simulated spectra of **1** and **3**; forbidden transitions (below 5 T) are shown by asterisks. Top and bottom panels: simulated energy levels of the ($S = 1.5$) Cr^{3+} monomer (**1**) and ($S = 2$) $Cr^{4+}-O-Cr^{4+}$ dimer (**3**), respectively, when the field is parallel to the z-axis. In both the top and bottom panels, the energy levels are labeled by their corresponding spin quantum numbers (M_S). All transitions are shown by vertical red bars, and the dotted lines point to the relevant peaks in the simulated spectrum. For clarity, only the peaks corresponding to molecular z-orientation are shown by dotted lines: z_1 and z_1' are from **1**, and z_2 and z_2' are from **3**.

Figure 15 depicts a simulated 240 GHz energy level diagram of **1** (top panel) and **3** (bottom panel) at 4.5 K. The vertical red bars mark the possible spin transitions, while the dotted lines point to the relevant peaks corresponding to molecular z-orientation (z_1 and z_1'; z_2 and z_2') in the simulated spectrum (center panel). The asterisks denote the spin forbidden transitions.

Proposed Mechanism for O_2 Activation. The reaction orders in [**1**], [O_2], [**2**], and [THF] are consistent with the proposed

Scheme 4. Proposed Mechanism for O_2 Activation by 1

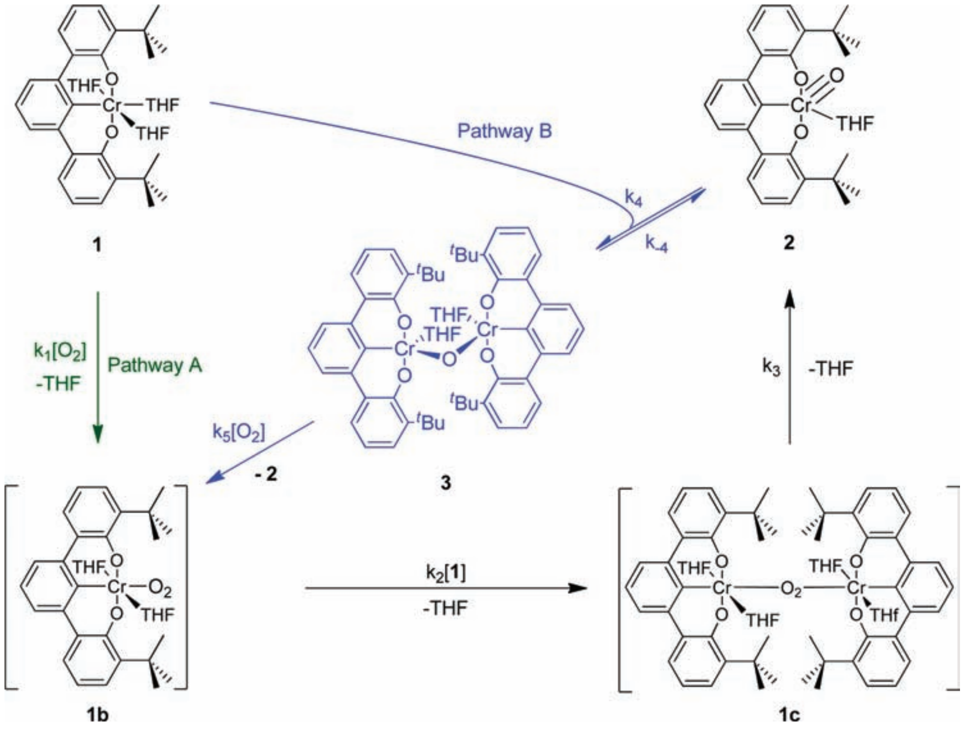

mechanism in Scheme 4. During the initial stages of the reaction, the oxidation of **1** follows pathway A. The first step involves the dissociation of THF followed by O_2 coordination to generate an intermediate species **1b**. A single-crystal X-ray structural analysis of **1** suggests preferential dissociation of the THF *trans* to the $Cr-C_{ipso}$ bond. Inspection of the three Cr−THF bond lengths in **1** reveals the $Cr-THF_{trans}$ (Cr1−O3 = 2.1939(18) Å) is ∼0.14 Å longer than the two $Cr-THF_{cis}$ bonds (Cr1−O4 = 2.0624(18) Å and Cr1−O5 = 2.0566(18) Å).[95]

It is proposed that intermediate species **1b** then reacts with **1** to generate a second intermediate **1c** before the O−O bond cleaves in the final step to yield **2**. The first-order dependence on [**1**] suggests that the formation of **1b** is the rate-determining step. The high rate of oxidation precludes definitive assignment for the structure of intermediates **1b** and **1c**. There are precedents for both end-on and side-on dioxygen−chromium complexes.[121−134]

To be autocatalytic, a product-catalyzed pathway has to accelerate the formation of **1b** to increase the overall rate of the oxidation. Pathway B in Scheme 4 illustrates the product-catalyzed oxidation of **1**. The formation of dimer **3** from **2** and **1** provides a low-coordinate species that allows O_2 access to the metal. The coordination of O_2 to **3** results in the cleavage of the dimer to yield **1b** and regenerates **2**, which can re-enter pathway B. Pathway B is faster than pathway A because pathway A requires the slow dissociation of THF prior to O_2 coordination, and thus autocatalytic conditions establish as the concentration of **2** increases.

Few of the previous studies that propose competent μ-oxo Cr and Mn dimer species in oxidation catalysis were able to assess whether the dimers participate in OAT to substrate.[55,57,60] Offering a chance to examine this directly, complex **3** was tested as an OAT transfer agent. Figure 16 depicts the time-dependent decay of complex **3** in the presence of PPh_3 (1.10, 2.21, and 4.42 ($\times 10^{-3}$) M). The data clearly indicate a zero-order dependence on the concentration of PPh_3, suggesting complex **3** must first break apart into mononuclear Cr^{III} (**1**) and $Cr^{V}(O)$ (**2**) prior to OAT.

Kinetic Simulations. Strong evidence exists for the autocatalytic pathway B, for example, the shape of the decay plots for the oxidation of **1** and, foremost, the isolation and characterization of dimer **3**. However, during the oxidation of **1**, dimer **3** is a steady state intermediate, and no experiment directly probes its formation. To complement the kinetic studies and to support the proposed mechanism, numerical simulations were performed using the computer program Kinetica. Equation 2 describes the stoichiometric reaction between **1** and O_2 to provide **2**, and eqs 3−7 show the elementary reaction steps from the proposed mechanism used in the simulations.

$$1 \xrightarrow{k_1[O_2]} 1b \tag{2}$$

$$1b + 1 \xrightarrow{k_2} 1c \tag{3}$$

$$1c \xrightarrow{k_3} 2 \tag{4}$$

$$2 + 1 \xrightarrow{k_4} 3 \tag{5}$$

$$3 \xrightarrow{k_{-4}} 2 + 1 \tag{6}$$

$$3 \xrightarrow{k_5[O_2]} 2 + 1b \tag{7}$$

The elementary steps involving the addition or dissociation of THF are excluded from the simulation. Since $[O_2]$ is in 10-fold excess, $k_1[O_2]$ and $k_5[O_2]$ are pseudo-first-order rate constants.

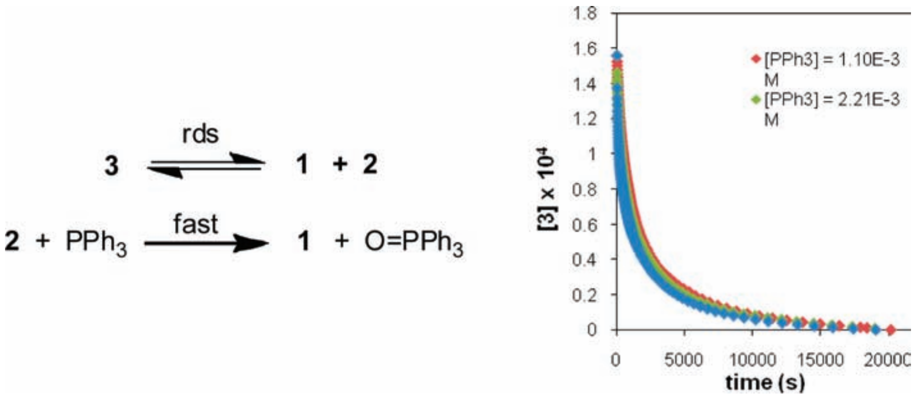

Figure 16. Left: Reaction sequence for dissociation of **3** (1.56×10^{-4} M) into **1** and **2** and the subsequent oxidation of PPh_3 ($1.10-4.42 \times 10^{-3}$ M) in CH_2Cl_2 (25 °C). Right: corresponding concentration (**3**) vs time (s) profile.

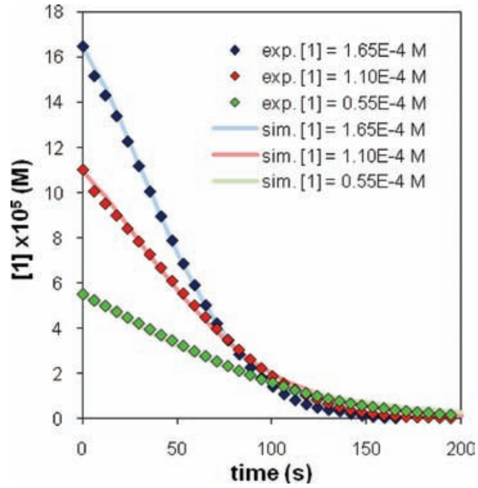

Figure 17. Simulated [**1**] ($0.55-1.65 \times 10^{-4}$ M) vs time (s) at [O_2] = 1.66×10^{-3} M. Correlation (R^2) values of simulated and experimental trials at 0.55×10^{-4} M **1** (0.999), 1.10×10^{-4} M **1** (0.999), and 1.65×10^{-4} M **1** (0.999) (THF, 25 °C).

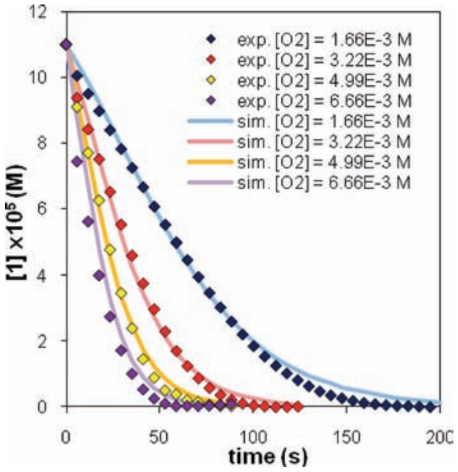

Figure 18. Simulated [**1**] (1.10×10^{-4} M) vs time (s) at different concentrations of [O_2] ($1.66-6.66 \times 10^{-3}$ M). Correlation (R^2) values of simulated and averaged experimental trials at 1.66×10^{-3} M O_2 (0.999), 3.33×10^{-3} M O_2 (0.998), 4.99×10^{-3} M O_2 (0.999), and 6.66×10^{-3} M O_2 (0.995) (THF, 25 °C).

Table 1. Average Calculated Rate Constants for the Oxidation of 1 (1.84×10^{-4} M) with O_2 (1.66×10^{-3} M) in THF at 25, 20, and 0 °C

T (°C)	25	10	0
k_1 (s^{-1})	2.6(±0.6)	1.2(±0.1)	0.5(±0.3)
k_4 ($M^{-1}s^{-1}$)	396.8(±0.7)	179(±8)	50(±9)
k_{-4}/k_5	6.1(±2.3) × 10−3	$2.9(\pm 0.4) \times 10^{-3}$	$1.8(\pm 0.6) \times 10^{-3}$

Equation 8 is the derived rate law for the set of eqs 3−7 and the proposed mechanism in Scheme 4 (see Supporting Information for details).

$$-\frac{d[\mathbf{1}]}{dt} = 2k_1[\mathbf{1}][O_2] + \frac{2k_4k_5[O_2][\mathbf{1}][\mathbf{2}]}{k_{-4} + k_5[O_2]} \qquad (8)$$

At each concentration of **1** (0.55, 1.10, and 1.65 ($\times 10^{-4}$) M) and O_2 (1.66, 3.33, 4.99, and 6.66 ($\times 10^{-3}$) M), three independent concentration versus time profiles were recorded. Using average concentration versus time data from the kinetic trials at each initial [**1**] and [O_2], the conjugate gradient optimization (see Supporting Information) provides the best fit rate constants. The rate constants k_2 and k_3 are indeterminable since they occur after the rate-determining step, and their values were fixed >1.00×10^6. The averaged estimated rate constants (k_1, k_4, k_{-4}/k_5) are 2.6(±0.6) s^{-1}, 396.8(±0.7) M^{-1} s^{-1}, and $6.0(\pm 2.3) \times 10^{-3}$, respectively (THF, 25 °C). Data fitting only permits the calculation of k_{-4}/k_5 as a ratio for the proposed mechanism. The rate constants were used to simulate individual concentration versus time profiles for kinetic runs that vary in the initial concentration of **1** and O_2. Figures 17 and 18 illustrate the simulated kinetic profile, and the experimental data, for concentration versus time profiles of **1** at different initial concentrations of **1** and O_2. The simulated kinetic profiles match the profiles obtained experimentally.

For the kinetic profiles varying in temperature, new rate constants were calculated for each temperature and are presented in Table 1. Figure 19 depicts the simulated and experimental concentration versus time profile for the oxidation of **1** with O_2 at different temperatures. An important feature exhibited in this set of data is the curvature of the profile at early reaction times. In particular, at 0 °C the reaction slows enough to detect the onset of the autocatalytic pathway B. The simulated data fit the experimental data well during

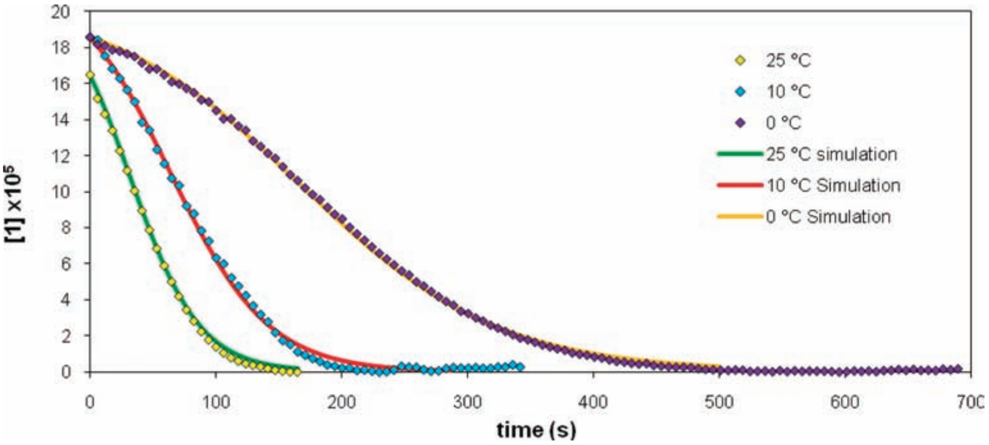

Figure 19. Simulated [**1**] vs time for the oxidation of **1** (1.65×10^{-4} M and 1.84×10^{-4} M) with O_2 (1.66×10^{-3} M) using the average calculated rate constants from Table 1.

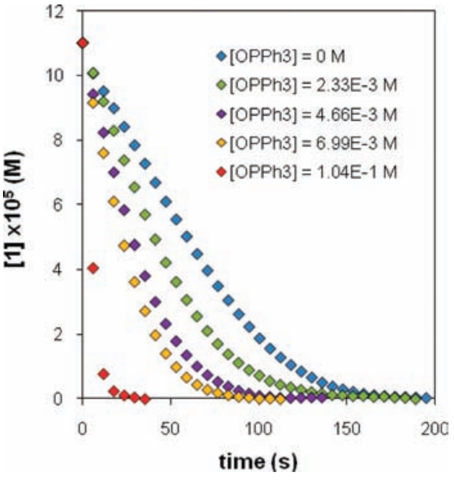

Figure 20. Plot of [**1**] vs time with increasing [$OPPh_3$] (0−0.1 M). [O_2] = 1.66×10^{-3} M and [**1**] = 1.10×10^{-4} M (THF, 25 °C).

Scheme 5

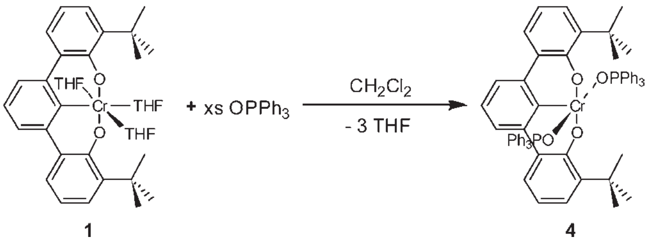

this stage of the reaction. At 40 °C, the reaction is too fast (only three data points within 10 s, >90% conversion) to obtain reliable data.

Inhibition Studies. Product inhibition occurs when a strong coordinating ligand/product binds to the metal center preventing further O_2 activation. The pincer architecture provides a labile coordination site via the strong *trans*-effect of the chromium−carbon bond and obviates catalyst deactivation by product inhibition. Complex **1** catalyzes the oxidation of PPh_3 to $OPPh_3$ with O_2 as the terminal oxidant.[95] In the case of Cr-corroles, the product $OPPh_3$ binds to the two axial positions thus inhibiting further oxidation.[135] Uniquely for the trianionic pincer complex **1**, the opposite occurs: an increasing concentration of $OPPh_3$ accelerates O_2 activation. Figure 20 contains a plot of the change in concentration of **1** versus time during the O_2 oxidation in the presence varying [$OPPh_3$] (0−0.10 M). The rate of oxidation of **1** accelerates upon addition of $OPPh_3$, and at 1000 equiv of $OPPh_3$ (0.10 M) the rate cannot be measured within our experimental setup.

The role of $OPPh_3$ in facilitating O_2 activation by **1** is similar to the role of complex **2** in the formation of the dimer **3**. Excess $OPPh_3$ provides the coordinatively unsaturated complex [^{t}BuOCO]$Cr^{III}(OPPh_3)_2$ (**4**) (Scheme 5). The solid state structure[95] indicates only two $OPPh_3$ ligands coordinate to the Cr^{III} ion despite excess $OPPh_3$ being present in solution. Complex **4** provides an unobstructed coordination site for O_2 coordination allowing for faster oxidation.

The increased rate of O_2 activation by adding $OPPh_3$ suggests an equilibrium between **1** and **4** exists in THF. As more $OPPh_3$ is added, the equilibrium shifts toward **4** until it is the dominant species. Attempts to directly monitor the rate of O_2 activation with **4** failed because the reaction is too fast.

Cyclic Voltammetry of 1, 3, and 4. Both dimer **3** and complex **4** have an open coordination site compared to **1**. As a consequence, the rate of O_2 activation is faster for **3** and **4**. However, the increased oxidation rate may be a consequence of a more reducing metal ion caused by the coordination of **2** in the dimer **3** and $OPPh_3$ in complex **4**. To examine this possibility, complexes **1**, **3**, and **4** were subjected to cyclic voltammetry experiments to determine their electrode potentials. Complexes **1**, **3**, and **4** display irreversible first oxidation peaks at 0.732, 0.298, and 0.012 V, respectively (see Supporting Information). Though the lower oxidation potentials appear to correlate with the faster rate of O_2 activation, the irreversibility of the CV spectra prevents a definitive conclusion from being drawn.

■ CONCLUSION

Trianionic pincer ligands offer an advantage over traditional meridional-tetradentate ligands for oxidation catalysis. One limitation of meridional-tetradentate ligands is catalyst deactivation by product inhibition or μ-O dimerization. Here, we describe the chromium(III) complex, [^{t}BuOCO]$Cr^{III}(THF)_3$ (**1**), that is not susceptible to these deactivation pathways. The kinetic results for

Scheme 6. New General Mechanism for Substrate Oxidation That Includes Reversible Formation of a M−O−M Intermediate

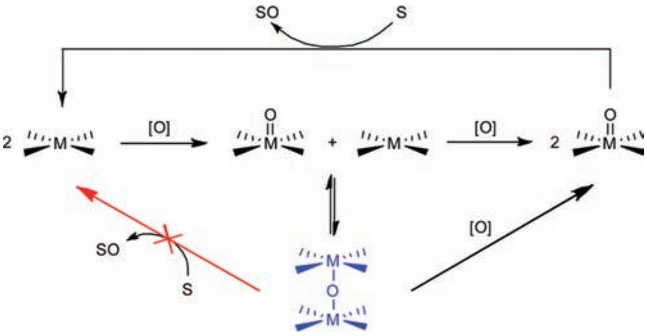

the oxidation of **1** reveal a first-order dependence in the initial concentration of **1** and O_2 and inverse order dependence in THF. However, plots of [**1**] and [O_2] vs time do not conform to standard first-order decay. The decay of **1** vs time remains linear for the first 80% of the reaction before tapering off. Lowering the temperature of the reaction for the oxidation of **1** yields a sigmoidal curve, indicative of an autocatalytic mechanism.

We establish conclusively the role product **2** plays in accelerating the O_2 activation. Adding equimolar amounts of **1** and **2** in toluene yields the μ-O dimer **3**. The single-crystal X-ray structure of **3** contains two tbp Cr^{IV} ions bridged by a μ-oxo. Each Cr^{IV} ion is coordinatively unsaturated and is partly responsible for the increased reactvity toward O_2, by providing an available coordination site for O_2 attack. Kinetic simulations support the proposed autocatalytic mechanism, in which complex **3** reacts directly with O_2 to form intermediate **1b** and reforms **2**. In contrast to iron(II) porphyrin catalysts that can deactivate by dimerization, the dimerization of **1** and **2** results in the formation of the *more reactive* complex **3**, thus establishing autocatalytic conditions.

In an attempt to simulate other product acceleration conditions, $OPPh_3$ was added to the kinetic oxidation trials and was found to increases the rate of O_2 activation by **1**. To further understand the role of $OPPh_3$ in facilitating O_2 activation by **1**, excess $OPPh_3$ was added to **1**, which yielded **4**. The single-crystal X-ray structure of **4** reveals a square pyramidal geometry consisting of two $OPPh_3$ ligands, one above and one below the plane of the ^{t}BuOCO^{-3} pincer ligand.[95] Similar to **3**, complex **4** is more reactive toward O_2 than complex **1** due to the open coordination site *trans* to the $Cr-C_{ipso}$ bond, which affords O_2 easier access to the metal center. This result implies trianionic pincer ligands, by virtue of only binding to three coordination sites, create inherently kinetically reactive complexes.

Finally, dimer **3** adds suppport to the longstanding contention that within Cr and Mn oxidation catalysts M−O−M species are involved but do not completely surpress reactivity. Complex **3** is the first crystallographically characterized dinuclear $Cr^{IV}-O-Cr^{IV}$ complex. Perhaps more importantly, EPR data (peak positions and the *g*, *D*, and *E* parameters) establish a characteristic fingerprint for d^2-d^2, $Cr^{IV}-O-Cr^{IV}$ species that can form in situ during catalysis. The EPR data may greatly enhance other research seeking to understand the acitivty of Cr oxidation catalysts where such species are viable but not isolable. For example, Theopold and co-workers report one other μ-O$[Cr^{IV}]_2$ dimer,[108] but only paramagnetically broadened ^{1}H NMR and IR data support the assignment. Kinetic analysis of OAT reactions employing Mn−O−Mn and Cr−O−Cr species indicates the dimers do not transfer an oxygen atom directly to the substrate. Instead, the dimer must break apart, and then the OAT occurs. Our study provides additional evidence that O-atom transfer indeed occurs post dimer cleavage. For the first time, we were able to directly monitor the decay of an isolable $Cr^{IV}-O-Cr^{IV}$ species during O-atom tranfer to substrate (PPh_3). Kinetic data reveal zero-order dependence in [PPh_3], implying the dimer cleaves prior to OAT. A more detailed mechanism for catalyst oxidation and OAT than the one depicted in Scheme 1 can be described for this system. We now include that M−O−M species can directly react with oxidant,[87,136] and we provide additional support that the direct OAT from a μ-O dimer is not plausible (Scheme 6). Current studies focus on generating more reactive M═O species using modified trianionic pincer ligands to increase the substrate scope of aerobic oxidation.

EXPERIMENTAL SECTION

General Procedure. Unless specified otherwise, all manipulations were performed under an inert atmosphere using standard Schlenk or glovebox techniques. Pentane, hexanes, toluene, dichloromethane, tetrahydrofuran (THF), and 1,2-dimethoxyethane (DME) were dried using a GlassContour drying column. Benzene-d_6 (Cambridge Isotopes) was dried over sodium-benzophenone ketyl, distilled or vacuum transferred, and stored over 4 Å molecular sieves. $[^t\mathrm{BuOCO}]\mathrm{Cr}^{III}(\mathrm{THF})_3$ (**1**), $[^t\mathrm{BuOCO}]\mathrm{Cr}^{V}(\mathrm{O})(\mathrm{THF})_3$ (**2**), and $[^t\mathrm{BuOCO}]\mathrm{Cr}^{III}(\mathrm{OPPh}_3)_2$ (**4**) were prepared according to published procedures.[95] All other reagents were purchased from commercial vendors and used without further purification. NMR spectra were obtained on Varian Gemini 300 MHz, Varian Mercury Broad Band 300 MHz, or Varian Mercury 300 MHz spectrometers. Chemical shifts are reported in δ (ppm). For ^{1}H and $^{13}C\{^1H\}$ NMR spectra, the solvent peak was referenced as an internal reference. Infrared spectra were obtained on a Thermo Scientific Nicolet 6700 FT-IR.

UV−vis spectra were acquired on a Hewlett-Packard 8453 spectrometer, and variable temperature was maintained using Fisher Scientific Isotemp 10065. Oxygenated solvents were prepared by bubbling O_2 through the solvent for 30 min and stored under an atmosphere of O_2 for 6 h before use. The concentration of O_2 was taken to be the accepted literature value.[104] The reference absorbance was used as the initial concentration absorbance prior to reagent injection. A trend line was fitted to the first 80% of the reaction progress and then used to extrapolate the observed rate. Spectra were acquired in quartz cuvettes with septum caps.

Electrochemical experiments were performed at ambient temperature in a glovebox using an EG&G PAR model 263A potentiostat/galvanostat and a three-compartment H-cell separated by a medium porosity sintered glass frit. Electrolytic solutions consisted of 0.1 M tetrabutylammonium hexafluorophosphate (TBAH) dissolved in either CH_2Cl_2 or THF. Cyclic voltammograms (CV) were recorded at 100 mV s^{-1} in 4 mL of electrolytic solution with 5×10^{-3} M complex concentration. A glassy carbon electrode (3 mm diameter) was used as the working electrode and a platinum flag as the counter electrode. All potentials are reported versus SCE and referenced to Ag/Ag$^+$. The reference electrode consisted of a silver wire immersed in a freshly prepared acetonitrile solution of 0.01 M $AgNO_3$ and 0.1 M TBAH encased in a 75 mm glass tube with a fitted Vycor tip. The *E*° values for the Fc$^+$/Fc couple in CH_2Cl_2 and THF were +0.47 V and +0.58 V versus SCE, respectively.[137]

Kinetic Simulations. Kinetic simulations were fitted using Kinetica version 1.0.17. The simulated rate constants were obtained by fitting the experimental trials using a conjugate gradient optimization with default convergence criterion of 0.01 and a dampening factor for simplex of 0.9.

Formation of $\{[^tBuOCO]Cr^{IV}(THF)\}_2(\mu\text{-}O)$ (3). Complex **1** (0.210 g, 3.28 × 10^{-4} mol) was dissolved in 5 mL of toluene. One-half of the solution (2.5 mL) was placed in a separate Schlenk flask and stirred under an atmosphere of anhydrous O_2 for 1 h to form **2** as a red solution. The solution of **2** was evaporated to provide a red powder, which was brought into a glovebox. The toluene solutions of **1** and **2** were combined yielding a deep purple color, and then the solvent was evaporated to yield a purple powder. ^1H NMR (300 MHz, C_6D_6): $\delta = 28.70$ ($\nu_{1/2} = 570$ Hz), 16.89 ($\nu_{1/2} = 675$ Hz), 13.38, 1.79, and −30.57 ($\nu_{1/2}$ = 540 Hz) ppm. The powder was dissolved in minimal Et_2O and cooled to −35 °C, yielding purple crystals of **3** and a few green crystals of **1**.

[1] vs Time: Oxidation of 1 with O_2 in THF. A 50 mL stock solution of **1** (21.2 mg, 3.31 × 10^{-5} mol) in THF was prepared. [**1**] variation: in the sample cells, 0.25, 0.5, and 0.75 mL of stock solution of **1** was diluted with 2.25, 2.0, and 1.75 mL of THF, respectively. Oxygenated THF (0.5 mL) was added to the sample cell via syringe, and the absorbance was monitored at 341 nm for 400 s. [O_2] variation: similarly, 0.5 mL of stock solution of **1** was diluted with 1.5, 1.0, and 0.5 mL of THF, and 1.0, 1.5, and 2.0 mL of oxygenated THF was added, respectively. [THF] variation: 0.5 mL of stock solution of **1** was diluted with 1.5, 1.0, and 0.5 mL of THF and 0.5, 1.0, and 1.5 mL of hexanes, respectively, and then 0.5 mL of oxygenated THF was added. [$OPPh_3$] variation: 20 mL of stock solution of $OPPh_3$ (73.3 mg, 2.63 × 10^{-4} mol) in THF was prepared. A stock solution (0.5 mL) of **1** was diluted with 0.5, 1.0, and 1.5 mL of THF and 1.5, 1.0, and 0.5 mL of $OPPh_3$ solution, and then 0.5 mL of oxygenated THF was added to the samples. [**2**] variation: 10 mL of stock solution of **1** was exposed to an atmosphere of O_2 for 0.5 h. The solution was dried under vacuum and redissolved in 10 mL of THF under an inert atmosphere. Samples containing 0.5 mL of stock solution of **1** were prepared using 0.25 and 0.5 mL of a stock solution of **2** with 1.75 and 1.5 mL of THF, respectively, and then 0.5 mL of oxygenated THF was inserted into the samples.

Variable Temperature: Oxidation of 1 with O_2 in THF. A 25 mL stock solution of **1** (22.3 mg, 3.48 × 10^{-5} mol) in THF was prepared. In the sample cell, 0.4 mL of the stock solution of **1** was diluted with 2.1 mL of oxygen-free THF. Oxygenated THF (0.5 mL) was then added to the reaction cell via syringe, and the absorbance was monitored at 341 nm for 300 s. The temperatures for the sample cells were set to 42, 25, 9, and −2 °C, and then 0.5 mL of ambient temperature oxygenated THF was added, resulting in a temperature change of 1−2 °C. As a result, the temperatures were taken to be 40, 20, 10, and 0 °C. Between kinetic trials, the temperature was re-equilibrated to the initial thermal value. Special considerations were taken for 0 °C trials in which a nitrogen-filled atmosphere was used to prevent ice formation on the cuvette. Also for 10 °C trials, the cuvette was periodically wiped to avoid water condensation.

[PPh_3] vs k_{obs}: OAT from $\{[^tBuOCO]Cr^{IV}(THF)\}_2(\mu\text{-}O)$ to PPh_3 in CH_2Cl_2. Stock solutions (25 mL) of **3** (47.0 mg, 4.68 × 10^{-5} mol) and PPh_3 (43.5 mg, 1.66 × 10^{-4} mol) in CH_2Cl_2 were prepared. Sample solutions were prepared using 0.25 mL of **3** by diluting with 2.25, 1.75, and 0.75 mL of CH_2Cl_2. These solutions were treated with 0.5, 1.0, and 2.0 mL of PPh_3, respectively, via syringe, and the absorbance was monitored at 850 nm for 6 h.

■ ASSOCIATED CONTENT

Ⓢ Supporting Information. Crystallographic, EPR spectra, ^1H NMR data for **3**, and rate law derivation. This material is available free of charge via the Internet at http://pubs.acs.org.

■ AUTHOR INFORMATION

Corresponding Author
veige@chem.ufl.edu

■ ACKNOWLEDGMENT

The authors thank UF, the ACS-PRF(G) (#44063-G3), NSF CAREER (CHE-0748408), the Camille and Henry Dreyfus Foundation, and the Alfred P. Sloan Foundation for financial support of this project. X-ray equipment was purchased with support from UF and the NSF (CHE-0821346). The EPR measurements were made at NHMFL which is supported by NSF and the State of Florida via the cooperative agreement DMR-0654418.

■ REFERENCES

(1) Wittcoff, H. A.; Reuben, B. G.; Plotkin, J. S. *Industrial Organic Chemicals*, 2nd ed.; John Wiley & Sons, Inc.: Hoboken, 2004.

(2) Weissermel, K.; Arpe, H.-J. *Industrial Organic Chemistry*, 4th ed.; Wiley-VCH: Weinheim, 2003.

(3) Centi, G.; Cavani, F.; Trifiro, F. *Selective Oxidation by Heterogeneous Catalysis*; Kluwer Academics/Plenum Publishers: New York, 2001.

(4) Backvall, J.-E. *Modern Oxidation Methods*; Wiley-VCH: Weinheim, 2004.

(5) Caron, S.; Dugger, R. W.; Ruggeri, S. G.; Ragan, J. A.; Ripin, D. H. B. *Chem. Rev.* **2006**, *106*, 2943–2989.

(6) Constable, D. J. C.; Dunn, P. J.; Hayler, J. D.; Humphrey, G. R.; Leazer, J. L.; Linderman, R. J.; Lorenz, K.; Manley, J.; Pearlman, B. A.; Wells, A.; Zaks, A.; Zhang, T. Y. *Green Chem.* **2007**, *9*, 411–420.

(7) Sheldon, R. A.; Kochi, J. K. *Metal-Catalyzed Oxidations of Organic Compounds*; Academic Press: New York, 1981.

(8) Punniyamurthy, T.; Velusamy, S.; Iqbal, J. *Chem. Rev.* **2005**, *105*, 2329–2363.

(9) Funabiki, T. Oxygenases and Model Systems. In *Catalysis by Metal Complexes*; Kluwer: Dordrecht, 1997.

(10) Satoh, T.; Miura, M. *Chem.—Eur. J.* **2010**, *16*, 11212–11222.

(11) Liu, C.; Jin, L. Q.; Lei, A. W. *Synlett* **2010**, 2527–2536.

(12) Gligorich, K. M.; Sigman, M. S. *Chem. Commun.* **2009**, 3854–3867.

(13) Punniyamurthy, T.; Rout, L. *Coord. Chem. Rev.* **2008**, *252*, 134–154.

(14) Piera, J.; Backvall, J. E. *Angew. Chem., Int. Ed.* **2008**, *47*, 3506–3523.

(15) Li, B. J.; Yang, S. D.; Shi, Z. J. *Synlett* **2008**, 949–957.

(16) Ferreira, E. M.; Zhang, H. M.; Stoltz, B. M. *Tetrahedron* **2008**, *64*, 5987–6001.

(17) Beccalli, E. M.; Broggini, G.; Martinelli, M.; Sottocornola, S. *Chem. Rev.* **2007**, *107*, 5318–5365.

(18) Popp, B.; Stahl, S. In *Organometallic Oxidation Catalysis*; Meyer, F., Limberg, C., Eds.; Springer: Berlin/Heidelberg, 2007; Vol. 22, pp 149−189.

(19) Schultz, M. J.; Sigman, M. S. *Tetrahedron* **2006**, *62*, 8227–8241.

(20) Gligorich, K. M.; Sigman, M. S. *Angew. Chem., Int. Ed.* **2006**, *45*, 6612–6615.

(21) Stahl, S. S. *Angew. Chem., Int. Ed.* **2004**, *43*, 3400–3420.

(22) Meunier, B.; de Visser, S. P.; Shaik, S. *Chem. Rev.* **2004**, *104*, 3947–3980.

(23) Que, L.; Tolman, W. B. *Nature* **2008**, *455*, 333–340.

(24) Friedle, S.; Reisner, E.; Lippard, S. J. *Chem. Soc. Rev.* **2010**, *39*, 2768–2779.

(25) Murray, L. J.; Lippard, S. J. *Acc. Chem. Res.* **2007**, *40*, 466–474.

(26) Baik, M. H.; Newcomb, M.; Friesner, R. A.; Lippard, S. J. *Chem. Rev.* **2003**, *103*, 2385–2419.

(27) Tshuva, E. Y.; Lippard, S. J. *Chem. Rev.* **2004**, *104*, 987–1011.

(28) Costas, M.; Mehn, M. P.; Jensen, M. P.; Que, L. *Chem. Rev.* **2004**, *104*, 939–986.

(29) Veige, A. S.; Slaughter, L. M.; Wolczanski, P. T.; Matsunaga, N.; Decker, S. A.; Cundari, T. R. *J. Am. Chem. Soc.* **2001**, *123*, 6419–6420.

(30) Veige, A. S.; Slaughter, L. M.; Lobkovsky, E. B.; Wolczanski, P. T.; Matsunaga, N.; Decker, S. A.; Cundari, T. R. *Inorg. Chem.* **2003**, *42*, 6204–6224.

(31) Pietsch, M. A.; Hall, M. B. *Inorg. Chem.* **1996**, *35*, 1273–1278.

(32) Pietsch, M. A.; Couty, M.; Hall, M. B. *J. Phys. Chem.* **1995**, *99*, 16315–16319.

(33) Woo, L. K. *Chem. Rev.* **1993**, *93*, 1125–1136.

(34) Crestoni, M. E.; Fornarini, S.; Lanucara, F.; Warren, J. J.; Mayer, J. M. *J. Am. Chem. Soc.* **2010**, *132*, 4336–4343.

(35) Holm, R. H. *Chem. Rev.* **1987**, *87*, 1401–1449.

(36) Holm, R. H.; Donahue, J. P. *Polyhedron* **1993**, *12*, 571–589.

(37) Betley, T. A.; Wu, Q.; Van Voorhis, T.; Nocera, D. G. *Inorg. Chem.* **2008**, *47*, 1849–1861.

(38) McGarrigle, E. M.; Gilheany, D. G. *Chem. Rev.* **2005**, *105*, 1563–1602.

(39) Muzart, J. *Chem. Rev.* **1992**, *92*, 113–140.

(40) Venkataramanan, N. S.; Kuppuraj, G.; Rajagopal, S. *Coord. Chem. Rev.* **2005**, *249*, 1249–1268.

(41) Chin, D. H.; Lamar, G. N.; Balch, A. L. *J. Am. Chem. Soc.* **1980**, *102*, 5945–5947.

(42) Chin, D. H.; Balch, A. L.; Lamar, G. N. *J. Am. Chem. Soc.* **1980**, *102*, 1446–1448.

(43) Chin, D. H.; Lamar, G. N.; Balch, A. L. *J. Am. Chem. Soc.* **1980**, *102*, 4344–4350.

(44) Momenteau, M.; Reed, C. A. *Chem. Rev.* **1994**, *94*, 659–698.

(45) Xia, Q. H.; Ge, H. Q.; Ye, C. P.; Liu, Z. M.; Su, K. X. *Chem. Rev.* **2005**, *105*, 1603–1662.

(46) Bryliakov, K. P.; Talsi, E. P. *Chem.—Eur. J.* **2007**, *13*, 8045–8050.

(47) Egami, H.; Katsuki, T. *J. Am. Chem. Soc.* **2009**, *131*, 6082–6083.

(48) Chang, C. J.; Baker, E. A.; Pistorio, B. J.; Deng, Y. Q.; Loh, Z. H.; Miller, S. E.; Carpenter, S. D.; Nocera, D. G. *Inorg. Chem.* **2002**, *41*, 3102–3109.

(49) Pistorio, B. J.; Chang, C. J.; Nocera, D. G. *J. Am. Chem. Soc.* **2002**, *124*, 7884–7885.

(50) Rosenthal, J.; Pistorio, B. J.; Chng, L. L.; Nocera, D. G. *J. Org. Chem.* **2005**, *70*, 1885–1888.

(51) Rosenthal, J.; Luckett, T. D.; Hodgkiss, J. M.; Nocera, D. G. *J. Am. Chem. Soc.* **2006**, *128*, 6546–6547.

(52) Rosenthal, J.; Nocera, D. G. *Prog. Inorg. Chem.* **2007**, *55*, 483–544.

(53) Samsel, E. G.; Srinivasan, K.; Kochi, J. K. *J. Am. Chem. Soc.* **1985**, *107*, 7606–7617.

(54) Lee, W. A.; Yuan, L. C.; Bruice, T. C. *J. Am. Chem. Soc.* **1988**, *110*, 4277–4283.

(55) Garrison, J. M.; Bruice, T. C. *J. Am. Chem. Soc.* **1989**, *111*, 191–198.

(56) Daly, A. M.; Renehan, M. F.; Gilheany, D. G. *Org. Lett.* **2001**, *3*, 663–666.

(57) Bryliakov, K. P.; Talsi, E. P. *Inorg. Chem.* **2003**, *42*, 7258–7265.

(58) Venkataramanan, N. S.; Rajagopal, S.; Vairamani, M. *J. Inorg. Biochem.* **2007**, *101*, 274–282.

(59) Garrison, J. M.; Ostovic, D.; Bruice, T. C. *J. Am. Chem. Soc.* **1989**, *111*, 4960–4966.

(60) Zhang, R.; Horner, J. H.; Newcomb, M. *J. Am. Chem. Soc.* **2005**, *127*, 6573–6582.

(61) Nam, W.; Kim, I.; Lim, M. H.; Choi, H. J.; Lee, J. S.; Jang, H. G. *Chem.—Eur. J.* **2002**, *8*, 2067–2071.

(62) Feichtinger, D.; Plattner, D. A. *Chem.—Eur. J.* **2001**, *7*, 591–599.

(63) Bryliakov, K. P.; Babushkin, D. E.; Talsi, E. P. *J. Mol. Catal. A: Chem.* **2000**, *158*, 19–35.

(64) Bryliakov, K. P.; Babushkin, D. E.; Talsi, E. P. *Mendeleev Commun.* **2000**, 1–3.

(65) Feichtinger, D.; Plattner, D. A. *J. Chem. Soc., Perkin Trans. 2* **2000**, *5*, 1023–1028.

(66) Plattner, D. A.; Feichtinger, D.; El-Bahraoui, J.; Wiest, O. *Int. J. Mass Spectrom.* **2000**, *195/196*, 351–362.

(67) Feichtinger, D.; Plattner, D. A. *Angew. Chem., Int. Ed.* **1997**, *36*, 1718–1719.

(68) Jacobsen, E. N.; Deng, L.; Furukawa, Y.; Martinez, L. E. *Tetrahedron* **1994**, *50*, 4323–4334.

(69) Lee, R. W.; Nakagaki, P. C.; Bruice, T. C. *J. Am. Chem. Soc.* **1989**, *111*, 1368–1372.

(70) Nolte, R. J. M.; Razenberg, J. A. S. J.; Schuurman, R. *J. Am. Chem. Soc.* **1986**, *108*, 2751–2752.

(71) Smegal, J. A.; Hill, C. L. *J. Am. Chem. Soc.* **1983**, *105*, 3515–3521.

(72) Schardt, B. C.; Smegal, J. A.; Hollander, F. J.; Hill, C. L. *J. Am. Chem. Soc.* **1982**, *104*, 3964–3972.

(73) Schardt, B. C.; Hollander, F. J.; Hill, C. L. *J. Chem. Soc., Chem. Commun.* **1981**, 765–766.

(74) Srinivasan, K.; Michaud, P.; Kochi, J. K. *J. Am. Chem. Soc.* **1986**, *108*, 2309–2320.

(75) *Metalloporphyrins in Catalytic Oxidations*; Sheldon, R. A., Ed.; Marcel Dekker: New York, 1994.

(76) Geiss, A.; Keller, M.; Vahrenkamp, H. *J. Organomet. Chem.* **1997**, *541*, 441–443.

(77) Horner, O.; Anxolabehere-Mallart, E.; Charlot, M. F.; Tchertanov, L.; Guilhem, J.; Mattioli, T. A.; Boussac, A.; Girerd, J. J. *Inorg. Chem.* **1999**, *38*, 1222–1232.

(78) Meng, Q. G.; Wang, L. T.; Liu, Y. Z.; Pang, Y. *Acta Crystallogr., Sect. E: Struct. Rep. Online* **2008**, *64*, M63–U631.

(79) Vogt, L. H., Jr.; Zalkin, A.; Templeton, D. H. *Inorg. Chem.* **1967**, *6*, 1725–1730.

(80) Baffert, C.; Collomb, M.-N.; Deronzier, A.; Pecaut, J.; Limburg, J.; Crabtree, R. H.; Brudvig, G. W. *Inorg. Chem.* **2002**, *41*, 1404–1411.

(81) Ghosh, K.; Eroy-Reveles, A. A.; Olmstead, M. M.; Mascharak, P. K. *Inorg. Chem.* **2005**, *44*, 8469–8475.

(82) Triller, M. U.; Hsieh, W.-Y.; Pecoraro, V. L.; Rompel, A.; Krebs, B. *Inorg. Chem.* **2002**, *41*, 5544–5554.

(83) Chen, H.; Faller, J. W.; Crabtree, R. H.; Brudvig, G. W. *J. Am. Chem. Soc.* **2004**, *126*, 7345–7349.

(84) Lentz, D.; Akkerman, F.; Kickbusch, R.; Patzschke, M. *Z. Anorg. Allg. Chem.* **2004**, *630*, 1363–1366.

(85) Gafford, B. G.; Holwerda, R. A.; Schugar, H. J.; Potenza, J. A. *Inorg. Chem.* **1988**, *27*, 1126–1128.

(86) Di Vaira, M.; Mani, F. *Inorg. Chem.* **1984**, *23*, 409–412.

(87) Liston, D. J.; West, B. O. *Inorg. Chem.* **1985**, *24*, 1568–1576.

(88) Li, S.; Wang, S. B.; Zhang, F. L.; Tang, K. *Acta Crystallogr., Sect. E: Struct. Rep. Online* **2008**, *64*, M2–U95.

(89) Darensbourg, D. J.; Moncada, A. I.; Choi, W.; Reibenspies, J. H. *J. Am. Chem. Soc.* **2008**, *130*, 6523–6533.

(90) Heintz, R. A.; Ostrander, R. L.; Rheingold, A. L.; Theopold, K. H. *J. Am. Chem. Soc.* **1994**, *116*, 11387–11396.

(91) Ruppa, K. B. P.; Feghali, K.; Kovacs, I.; Aparna, K.; Gambarotta, S.; Yap, G. P. A.; Bensimon, C. *J. Chem. Soc., Dalton Trans.* **1998**, 1595–1606.

(92) Kuppuswamy, S.; Peloquin, A. J.; Ghiviriea, I.; Abboud, K. A.; Veige, A. S. *Organometallics* **2010**, *29*, 4227–4233.

(93) Kuppuswamy, S.; Ghiviriga, I.; Abboud, K. A.; Veige, A. S. *Organometallics* **2010**, *29*, 6711–6722.

(94) Sarkar, S.; McGowan, K. P.; Culver, J. A.; Carlson, A. R.; Koller, J.; Peloquin, A. J.; Veige, M. K.; Abboud, K. A.; Veige, A. S. *Inorg. Chem.* **2010**, *49*, 5143–5156.

(95) O'Reilly, M.; Falkowski, J. M.; Ramachandran, V.; Pati, M.; Abboud, K. A.; Dalal, N. S.; Gray, T. G.; Veige, A. S. *Inorg. Chem.* **2009**, *48*, 10901–10903.

(96) Golisz, S. R.; Labinger, J. A.; Bercaw, J. E. *Organometallics* **2010**, *29*, 5026–5032.

(97) Golisz, S. R.; Bercaw, J. E. *Macromolecules* **2009**, *42*, 8751–8762.

(98) Korobkov, I.; Gorelsky, S.; Gambarotta, S. *J. Am. Chem. Soc.* **2009**, *131*, 10406–10420.

(99) Sarkar, S.; Carlson, A. R.; Veige, M. K.; Falkowski, J. M.; Abboud, K. A.; Veige, A. S. *J. Am. Chem. Soc.* **2008**, *130*, 1116–1117.

(100) Sarkar, S.; Abboud, K. A.; Veige, A. S. *J. Am. Chem. Soc.* **2008**, *130*, 16128–16129.

(101) Agapie, T.; Day, M. W.; Bercaw, J. E. *Organometallics* **2008**, *27*, 6123–6142.

(102) Agapie, T.; Bercaw, J. E. *Organometallics* **2007**, *26*, 2957–2959.

(103) Koller, J.; Sarkar, S.; Abboud, K. A.; Veige, A. S. *Organometallics* **2007**, *26*, 5438–5441.

(104) Battino, R. *Oxygen and Ozone*; Pergamon: New York, 1981.

(105) Egorova, O. A.; Tsay, O. G.; Huh, J. O.; Churchill, D. G. *Inorg. Chem.* **2009**, *38*, 4634–4636.

(106) Meier-Callahan, A. E.; Gray, H. B.; Gross, Z. *Inorg. Chem.* **2000**, *39*, 3605–3607.

(107) Odom, A. L.; Mindiola, D. J.; Cummins, C. C. *Inorg. Chem.* **1999**, *38*, 3290–3295.

(108) Noh, S. K.; Heintz, R. A.; Haggerty, B. S.; Rheingold, A. L.; Theopold, K. H. *J. Am. Chem. Soc.* **1992**, *114*, 1892–1893.

(109) Collins, T. J.; Slebodnick, C.; Uffelman, E. S. *Inorg. Chem.* **1990**, *29*, 3433–3436.

(110) Morse, D. B.; Rauchfuss, T. B.; Wilson, S. R. *J. Am. Chem. Soc.* **1988**, *110*, 8234–8235.

(111) Srinivasan, K.; Kochi, J. K. *Inorg. Chem.* **1985**, *24*, 4671–4679.

(112) Herberhold, M.; Kremnitz, W.; Razavi, A.; Schollhorn, H.; Thewalt, U. *Angew. Chem., Int. Ed.* **1985**, *24*, 601–602.

(113) Krumpolc, M.; DeBoer, B. G.; Rocek, J. *J. Am. Chem. Soc.* **1978**, *100*, 145–153.

(114) Gahan, B.; Garner, D. C.; Hill, L. H.; Mabbs, F. E.; Hargrave, K. D.; McPhail, A. T. *J. Chem. Soc., Dalton Trans.* **1977**, 1726–1729.

(115) Addison, A. W.; Rao, T. N.; Reedijk, J.; van Rijn, J.; Verschoor, G. C. *J. Chem. Soc., Dalton Trans.* **1984**, 1349–1356.

(116) Money, J. K.; Folting, K.; Huffman, J. C.; Chistou, G. *Inorg. Chem.* **1987**, *26*, 944–948.

(117) Ozarowski, A. *SPIN*; National High Magnetic Field Laboratory: Tallahassee.

(118) Weil, J. A.; Bolton, J. R.; Wertz, J. E. *Electron Paramagnetic Resonance: Elementary Theory and Practical Applications*; Wiley-Interscience: New York, 1994.

(119) Kahn, O. *Molecular Magnetism*; VCH: New York, 1993.

(120) Abragam, A.; Bleaney, B. *Electron Paramagnetic Resonance of Transition Ions*; Oxford University Press: Oxford, England, 1970.

(121) Theopold, K. H. *Top. Organomet. Chem.* **2007**, *22*, 17–37.

(122) Sugawara, K.-i.; Hikichi, S.; Akita, M. *Dalton Trans.* **2003**, 4346–4355.

(123) Qin, K.; Incarvito, C. D.; Rheingold, A. L.; Theopold, K. H. *Angew. Chem., Int. Ed.* **2002**, *41*, 2333–2335.

(124) Pestovsky, O.; Bakac, A. *Dalton Trans.* **2005**, 556–560.

(125) Pestovsky, O.; Bakac, A. *J. Am. Chem. Soc.* **2003**, *125*, 14714–14715.

(126) Dickman, M. H.; Pope, M. T. *Chem. Rev.* **1994**, *94*, 569–584.

(127) Cramer, C. J.; Tolman, W. B.; Theopold, K. H.; Rheingold, A. L. *Proc. Natl. Acad. Sci. U.S.A.* **2003**, *100*, 3635–3640.

(128) Cho, J.; Woo, J.; Nam, W. *J. Am. Chem. Soc.* **2010**, *132*, 5958–5959.

(129) Bakac, A. *Inorg. Chem.* **2010**, *49*, 3584–3593.

(130) Bakac, A.; Wang, W. D. *J. Am. Chem. Soc.* **1996**, *118*, 10325–10326.

(131) Bakac, A.; Scott, S. L.; Espenson, J. H.; Rodgers, K. R. *J. Am. Chem. Soc.* **1995**, *117*, 6483–6488.

(132) Adams, A. C.; Crook, J. R.; Bockhoff, F.; King, E. L. *J. Am. Chem. Soc.* **1968**, *90*, 5761–5768.

(133) Nemes, A.; Pestovsky, O.; Bakac, A. *J. Am. Chem. Soc.* **2002**, *124*, 421–427.

(134) Bakac, A. *Coord. Chem. Rev.* **2006**, *250*, 2046–2058.

(135) Mahammed, A.; Gray, H. B.; Meier-Callahan, A. E.; Gross, Z. *J. Am. Chem. Soc.* **2003**, *125*, 1162–1163.

(136) Budge, J. R.; Gatehouse, B. M. K.; Nesbit, M. C.; West, B. O. *J. Chem. Soc., Chem. Commun.* **1981**, 370–371.

(137) Noviandri, I.; Brown, K. N.; Fleming, D. S.; Gulyas, P. T.; Lay, P. A.; Masters, A. F.; Phillips, L. *J. Phys. Chem. B* **1999**, *103*, 6713–6722.